Nicolás Antonio Ramos Ojeda
Matthias Kind*

A Comprehensive Workflow towards More Equant-Shaped Crystals of Active Pharmaceutical Ingredients

The morphology of crystalline active pharmaceutical ingredients (APIs) can significantly affect their product properties, so that its control during manufacturing is crucial. To address this, a newly augmented commercial milliliter-scale facility and knowledge-based workflow were developed with the aim of identifying optimal process conditions for producing more equant-shaped crystals. The design includes minimal material usage, inline imaging, and independent temperature and supersaturation control through evaporative crystallization. The methodology enables the identification of process conditions for equant-shaped crystals across diverse APIs. These findings contribute to advancing pharmaceutical research and development by providing a reliable approach to optimize crystal morphology.

Supporting Information available online

Keywords: Active pharmaceutical ingredients, Crystal morphology, Evaporative crystallization, Inline imaging, Miniaturization

Received: July 02, 2023; *revised:* November 17, 2023; *accepted:* December 11, 2023

DOI: 10.1002/ceat.202300314

1 Introduction

Batch crystallization plays an essential role in the pharmaceutical industry and occupies a significant part of the resources dedicated to research and development [1]. About 90 % of the active pharmaceutical ingredients (APIs) are produced as solids and are predominantly crystalline [2]. In this perspective, the control of the properties of the produced crystals have been investigated intensely and with special attention to the desired product quality [3, 4]. Among the many crystal properties, the crystal morphology, i.e., the external shape of a crystal, is one of the critical attributes. This property exerts important effects on the processability in downstream operations [5, 6] and the physicochemical behavior [7–10]. Given the relevance of the crystal morphology, extensive studies have been conducted over the years to elucidate fundamental relationships involved in the resulting crystal morphologies [11–13]. Presently, it is well accepted that solvent [14–16], temperature [17, 18], degree of supersaturation [19–21], and use of additives [22] are of potential relevance to the crystal morphology.

Comprehensive screening covering diverse combinations of these variables could aid in identifying the process conditions that lead to a determined crystal morphology. Crystal morphology prediction models [23, 24] and computer-aided tools [25–27] have been developed to foretell the resulting crystal morphologies. However, most of the available models aim at the simulation of the growth of single crystals [28, 29] under conditions far from those of typical batch stirred-solution crystallization. As a result, they are difficult to transfer to the prediction of the crystal morphology in bulk crystallization [30, 31]. Consequently, there is still a great need for experimental techniques in crystal morphology screening and control. This demand is even more pronounced for APIs in the early stages of their development, when only few crystallization data are available. For this reason, this work aims to address this need by introducing a robust experimental workflow tailored for the investigation of novel or barely known APIs. The objective is to identify precise process conditions that lead to desired morphologies, with a particular focus on achieving more equant shapes, as are typically desired.

The method proposed in this article is subject to the following requirements: (1) efficient usage of raw material, (2) good transferability for upscaling, and (3) unmistakable assessment of the crystal morphology with the process conditions. Although the above requirements are logically reasonable, they are only partially met in most morphological studies. First, there is a lack of small-scale experimental setups that closely resemble bulk crystallization. Second, in batch experiments there is frequent overlap of variables and hence an inherent difficulty in the interpretation of the obtained results. Third, often off-line evaluation of crystal morphology is carried out, which can be unreliable due to the necessary preparation steps.

To meet the above requirements, this study used an advanced miniaturized multi-reactor system (Crystalline, Technobis Co.) for bulk crystallization equipped with inline imaging. This device has been augmented to allow for

---

Nicolás Antonio Ramos Ojeda
https://orcid.org/0009-0006-1783-5313, Dr. Matthias Kind
(matthias.kind@kit.edu)
Karlsruhe Institute of Technology (KIT), Thermal Process Engineering (TVT), Kaiserstrasse 12, 76131 Karlsruhe, Germany.

controlled isothermal batch evaporative crystallization. The process conditions in the miniaturized reactors mimic rather well large-scale conditions in stirred crystallizers, facilitating upscaling. In addition, the miniaturization and parallelization contribute to designing extensive experimental plans with minimal API usage. In contrast to traditional batch cooling crystallization, the amended setup decouples temperature and supersaturation, simplifying interpretation of the dependencies of the crystal morphology on these variables. Finally, the inline imaging provides a clear and unambiguous relationship between crystal morphology and process variables by excluding potential changes from sampling and solid-liquid separation [32–35].

2 Materials

Three patented model APIs, namely Bitopertin (Form A) [36], Balapiravir Hydrochloride [37], and a DPP-IV Inhibitor (DPP-IV Inh) [38], generously provided by Hoffmann-La Roche Co. Basel, Switzerland, were made available with the specific goal of converting their primarily needle-like crystal morphology to more equant shapes. Their chemical structures along with exemplary microscopic images are depicted in Fig. 1.

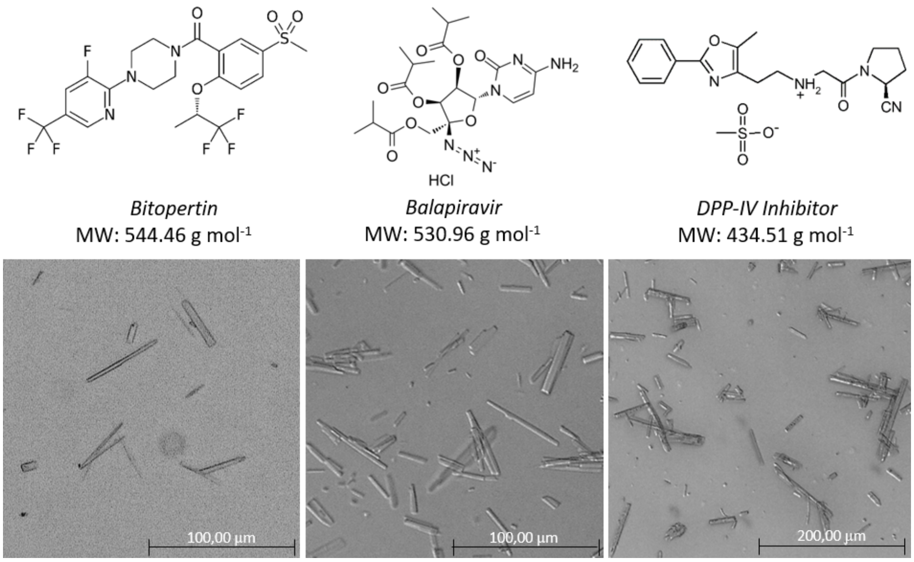

Figure 1. Structural formulas of the APIs used in this study along with exemplary microscopic images.

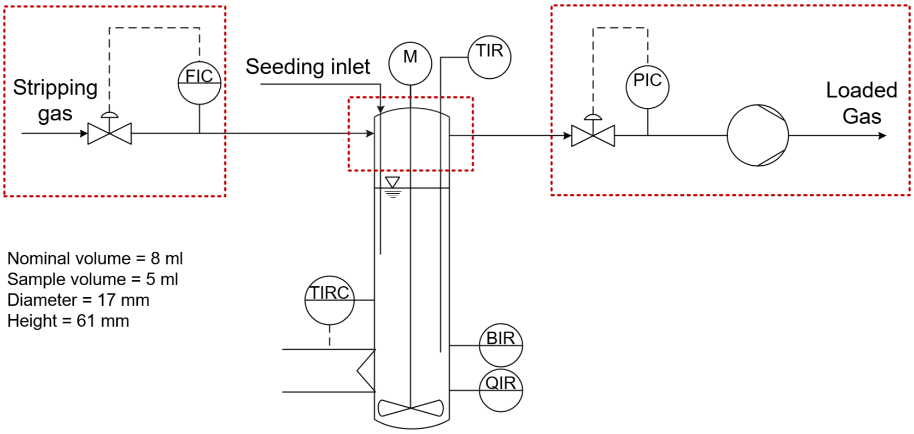

Figure 2. Experimental setup for one out of the eight crystallizers in Crystalline.

3 Methodology

3.1 Experimental Setup

Fig. 2 depicts the experimental setup for one of the eight independent reactors of the above-mentioned Crystalline crystallization system and illustrates the amendments implemented for controlled isothermal evaporation (delimited in red).

The standard device features: (1) temperature control within the range from –20 to 145 °C (TIRC), (2) controlled mixing (M) by means of a pitched four-blade overhead stirrer ($d_{\text{blade}} = 9$ mm) or by PTFE micro-stirring bars (rectangular, 10×3 mm) at the bottom of the glass vial, (3) transmissivity measurement across the reactor (QIR), and (4) visualization of the crystallization by internal CCD cameras (BIR). As the device lacks the capability for controlled evaporation, a concept for achieving isothermal evaporation using a stripping gas was developed. For this purpose, a gas flow (nitrogen) is fed to the vial and led over the surface of the liquid. To adjust the pressure, a vacuum pump (LVS 105 T – 10 ef, Welch Co.) was connected to the respective vacuum controller (Vacuu-Select controller, Vacuubrand Co., PIC) at each of the reactors. To set the stripping gas flow to each vial, thermal mass flow controllers (EL-Flow-Select, Bronkhorst Co., FIC) were installed at each reactor. Customized lids with four openings were used to allow the inlet and outlet of the gas and vapor, as port for feeding of seed crystals, and as opening for inserting a temperature sensor (TIR) into the vials.

3.2 Experimental Workflow

In order to successfully obtain more equant-shaped crystals of the selected APIs, a workflow to systematically cover the whole crystallization design was devised, starting from solvent selection and concluding with crystal morphology analysis by image analysis. The steps of the workflow are depicted in Fig. 3 and described in the following sections.

3.2.1 Solvent Selection

The initial step in the presented workflow is to rationally select a manageable number of solvents for crystallization experiments. The selected solvents should fulfill three key criteria: (1) hazard-free level, based on ICH Q3C guidelines for residual solvents; (2) soluble (30–10 mL solvent/g API) or sparingly soluble (100–30 mL solvent/g API) behavior of the API according to the European Pharmacopeia [39], and (3) high dissimilarity of the selected pure solvents, as categorized, e.g., by Allesø et al. [40]. Further details of the solvent selection are given in the Supporting Information (see Sect. S1).

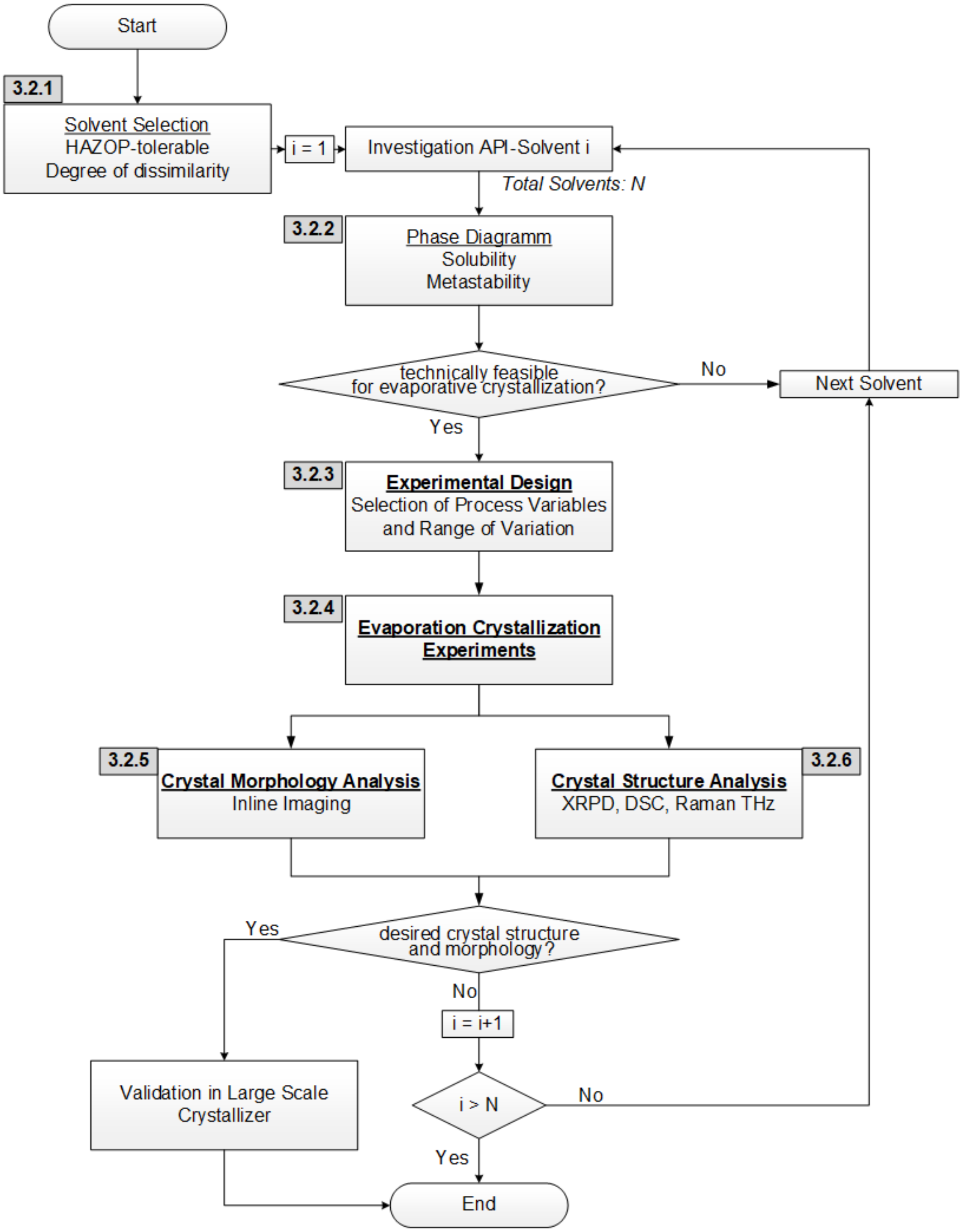

Figure 3. Experimental workflow for crystal morphology screening and manipulation. The numbering of the blocks indicates the dedicated subchapter in this article. DSC: differential scanning calorimetry, HAZOP: hazard and operability.

3.2.2 Phase Diagram

The second step involves determining the solubility and metastable zone limit (MZL) of the API-solvent binary systems to establish operational conditions for the evaporation crystallization experiments. In particular, temperature variation while acquiring the solution transmissivity emerged as an ideal option to obtain fast and reliable measurements. More extensive information about the technique is comprehensively detailed in other sources [41]. Details specific to this study are available in Sect. S2.

3.2.3 Experimental Design

In the third step of the workflow, the experimental design is set. Specifically, in this work the focus lies on four key factors that play a significant role in determining crystal morphology: (1) rate of supersaturation buildup, (2) crystallization temperature T_c, (3) use of seed crystals, and (4) solvent. The substantial miniaturization and the availability of multiple crystallizers in the chosen experimental setup make it possible to employ a full factorial experimental design to explore the desired factors. The precise experimental conditions investigated for each API are listed in Sect. S3.

3.2.4 Evaporative Crystallization

The innovative inclusion of controlled isothermal batch evaporative crystallization in the chosen miniaturized device allows independently the impact of the temperature and the supersaturation on the crystal morphology to be explored. In Fig. 4a, which provides an illustrative depiction of the process, the mass loading of the solvent at the end of an experiment X_E is set intentionally above the MZL to enable the probability of spontaneous crystallization. The initial mass loading of the solution X_0 is exactly half of X_E. Thus, when half of the solvent is evaporated, the solution reaches the target X_E value. To adjust the solutions to X_0 in the metastable state, the prepared suspensions are heated to the temperature T_d for dissolving all solid API. T_d is set 5 °C above the solubility temperature T^* of the solution. Thereafter, the clear solution is cooled down swiftly until the targeted crystallization temperature T_c is reached. If crystallization does not start before X_E is reached (after evaporation of 50 % of the solvent), further evaporation is permissible, but the sample volume should not be reduced to less than 1.5 mL. Otherwise, accurate inline imaging and measuring is hindered.

Fig. 4b depicts two exemplary cases of reaching X_E starting at the same X_0. In one case, the time to evaporate half of the solvent τ_{50} is 60 min, and in the other it is 210 min. Clearly, τ_{50} depends on the evaporation rate $\dot{m}_v$ [Eq. (1)], which in turn is determined by the temperature, pressure, solvent, and most importantly the stripping gas flow. Thereby, the course of mass loading and supersaturation can be calculated on the basis of $\dot{m}_v$; the detailed calculation is given in Sect. S4.

$$\tau_{50} = 0.5 \cdot \frac{m_{\text{solvent},0}}{\dot{m}_v} \tag{1}$$

For seeded experiments, the same methodology is proposed. Here, the inoculation is done shortly before the start of evaporation. It is emphasized that the seed material should be prepared to ensure a uniform and ideally isometric morphology to serve as a template. Further details of the seed preparation and the seeding itself are given in Sect. S5.

3.2.5 Morphology Analysis

The morphology analysis of the inline images derives from a standard procedure programmed in Matlab (details are given in Sect. S6). In this analysis, the morphology is quantified by the aspect ratio (AR), which is defined in Eq. (2) as the ratio between the major axis x_{max} and minor axis x_{min} of the ellipse

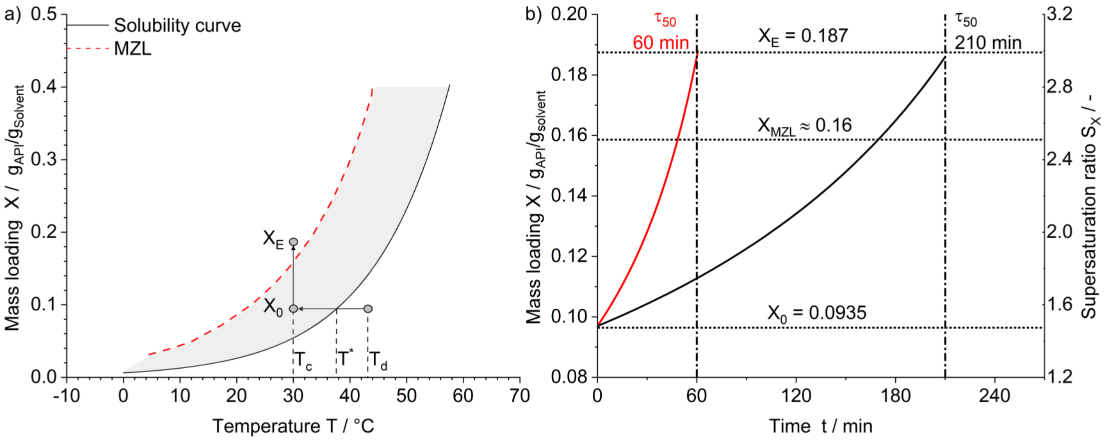

Figure 4. (a) Phase diagram of Bitopertin in ethanol with exemplary process route of evaporative crystallization experiments at 30 °C. (b) Course of supersaturation and mass loading of the solution for this process route, but for two different evaporation rates (τ_{50} = 60 and 210 min).

that contours the detected crystal. Furthermore, for a straightforward evaluation of the crystal morphology, its characterization is based on the median value of the aspect ratio $\mathrm{AR}_{50,0}$ resulting from the total number of crystals. The evaluation of $x_{\max}$ and $x_{\min}$ enables additionally the assessment of the crystal size distribution (CSD) along these two dimensions.

$$\mathrm{AR} = \frac{x_{\max}}{x_{\min}} \tag{2}$$

To ensure a fair comparison of $\mathrm{AR}_{50,0}$ across experiments, a practical range for image analysis must be defined. This range should encompass an assessment of both the increase in the number of detected particles N_p and the ratio of the projected area of the crystals to that of the total image $A_\mathrm{crystal}/A_\mathrm{image}$. In our experiments, the comparison of $\mathrm{AR}_{50,0}$ was performed at a specific point coinciding with a predetermined value of $A_\mathrm{crystal}/A_\mathrm{image}$, referred to as end image analysis. This approach guarantees that the data points correspond to suspensions with comparable crystal contents.

A qualitative comparison of the inline morphology and the final dried product is also proposed to assess potential alterations and identify the best option for upscaling. Conditions leading to a stable morphology after solid-liquid separation are favorable for evaluation at a larger scale. The procedure for the filtration and drying of the product suspensions is given in Sect. S7.

3.2.6 Crystal Structure Analysis

The crystalline product is analyzed to infer whether an observed change in crystal morphology is exclusively due to the change in the crystal growth rates of the different faces and is not due to a change in crystal structure. In this study, the samples were analyzed by X-ray powder diffraction (XRPD; D8 Advance, Bruker). The diffraction peak positions of the investigated samples were compared with those of the already known polymorphous forms.

4 Results and Discussion

4.1 Solvent Selection and Phase Diagrams

The proposed solvent selection method limited the number of solvents used in evaporative crystallization experiments for each API to three. Fig. 5a–c show the solubility curves and MZLs for the binary mixtures of the APIs with their respective solvents. Fig. 5 shows that the methodology worked as envisioned. Although the number of solvents is minimal, they provide a diverse landscape for crystallization, which, when combined with an experimental strategy that includes a wide range of process parameters, is more likely to influence the crystal morphology. The solubility curves result from the fitting of the measured points according to an exponential function

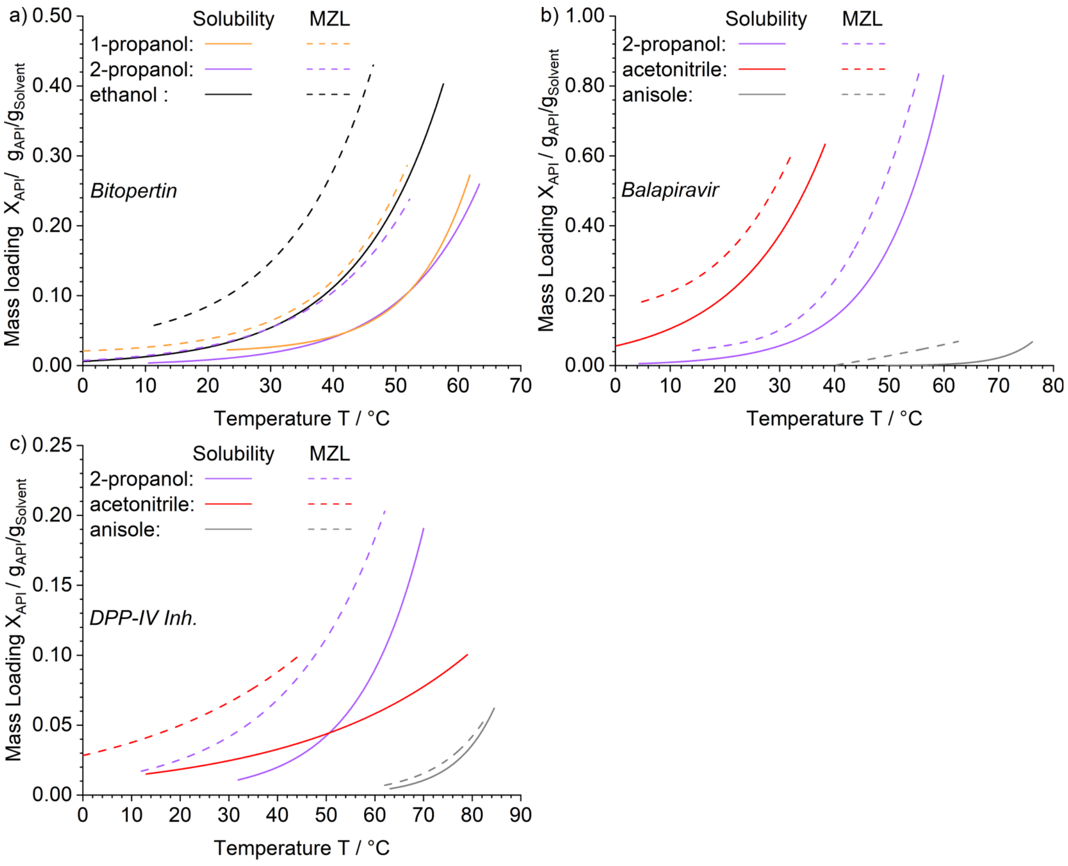

Figure 5. Solubility and MZL for API-solvent pairs. (a) Bitopertin, (b) Balapiravir, and (c) DPP-IV Inh.

[Eq. (3)]. On the other hand, each MZL was derived from the interpolation of the minimum undercooling required at each investigated mass composition. The measured data and the parameters $A_{i,j}$ and $B_{i,j}$ for each investigated binary system are presented in Sect. S8.

$$X^*_{ij} = A_{ij} \cdot e^{B_{ij} \cdot T/^\circ\mathrm{C}} \quad i\text{:solvent}; j\text{:API} \tag{3}$$

4.2 Bitopertin

To understand how the specific factors affect the crystal morphology, selected cases were focused on. These showcase differences and provide insights into the crystal morphology manipulation. The experimental conditions of these selected cases are given in Tab. 1 along with their resulting morphologies. The discussion focuses primarily on $AR_{50,0}$. The two-dimensional CSD in terms of x_{max} and x_{min}, which is of main interest for upscaling, is presented in a subordinate way in Sect. S9.

Fig. 6a shows representative sections of the images used for the AR evaluation. They show a variety of crystal morphologies ranging from perfect isometric crystals to undesirable needle-shaped ones. The cumulative frequency distribution of the aspect ratio $Q_{0,AR}$, (Fig. 6b) ranges from 1 to about 30. Furthermore, the morphology observed inline is very similar to that found for the dry product. Only in Cases V and VI do the crystals seem slightly less elongated after filtering and drying. However, more importantly, in both cases in which isometric crystals were detected inline (Cases II and IV), there is no substantial difference in the dry product.

Additionally, XRPD analysis ruled out the possibility of additional polymorph crystallization in any of the cases in Tab. 1. The stable polymorph (Form A) was always formed, demonstrating that the change in crystal morphology was obtained solely by a change in crystal growth influenced by the variation of the process conditions. The corresponding diffractograms are included in the supporting information (Sect. S10).

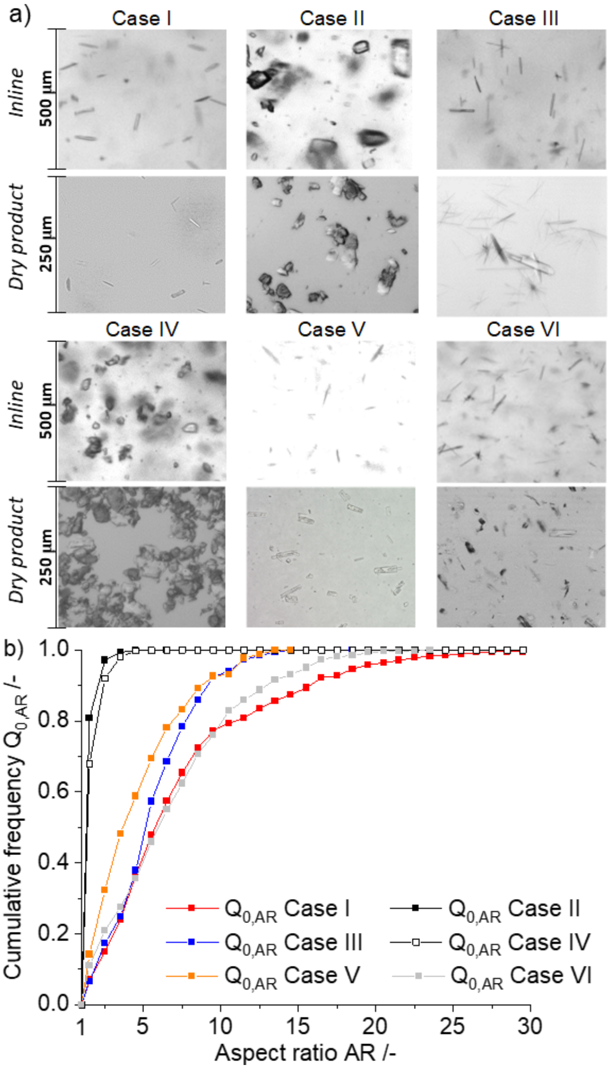

Figure 6. (a) Images acquired by Crystalline (inline) and after solid-liquid separation (dry product) for the crystal morphology analysis of the selected cases in Tab. 1. (b) Particle number based cumulative distribution of the AR for the cases presented in Tab. 1 based on the inline images. Isometric crystals tend to aspect ratios close to 1.

In summary, the experiments revealed favorable process conditions for producing more equant-shaped crystals. The produced crystals are also sufficiently robust to retain their morphology following solid-liquid separation and provide a promising pivot point for large-scale experiments. To clarify

Table 1. Experimental conditions and outcome of selected Bitopertin crystallization cases.

Case	Factor (1)		Factor (2)	Factor (3)	Factor (4)	S_0 [–]	S_{nucl} [–]	Crystal morphology	$AR_{50,0}$ [–]
	τ_{50} [h]	$\dot{m}_v$ [mg min^{-1}]	T [°C]	Unseeded/seeded	Solvent				
I	1.0	33	45	Unseeded	Ethanol	1.47	2.67	Needle	6.24
II	3.5	9	45	Unseeded	Ethanol	1.45	1.72	Isometric	1.55
III	3.5	9	30	Unseeded	Ethanol	1.48	2.10	Needle	5.26
IV	1.0	33	45	Seeded	Ethanol	1.33	1.60	Isometric	1.60
V	3.5	10	45	Unseeded	1-Propanol	1.47	2.85	Needle	3.54
VI	3.5	9	45	Unseeded	2-Propanol	1.52	2.60	Needle	4.38

and properly break down the factor(s) responsible for these morphological changes, the following subsections discuss selected experiments focusing on one variable at a time.

4.2.1 Effect of Evaporation Time/Rate of the Supersaturation Buildup (Factor 1)

A simple visual comparison between Cases I and II, both conducted in ethanol at 45 °C with varying evaporation rates, clearly illustrates the effect of this factor on the crystal morphology. Fig. 6a shows needle-shaped crystals that are formed in the case of fast supersaturation buildup (Case I), whereas isometric crystals are formed at slow supersaturation buildup (Case II). The corresponding quantitative evaluation of the AR distribution, which is presented in Fig. 6b, clearly captures the qualitative observations of the crystal morphology. For Case II, the AR tends to more isometric values in comparison with Case I.

In Case I nucleation starts at a higher supersaturation ratio and rapid evaporation continues to drive the supersaturation faster to higher values (Fig. 7). Thus, the crystal growth is subjected to higher supersaturation in comparison with Case II. Certainly, the supersaturation begins to decrease after nucleation. However, in the range of the image analysis, the calculated total mass of formed crystals is substantially smaller, as the total mass of API in the suspension and its impact on the supersaturation are negligible, this analysis is given in detail in Sect. S4.

From this result, it is deduced that a high evaporation rate (here: Case I) leads to nucleation onset and crystal growth at higher supersaturation ratios, compared with the cases in which evaporation is performed more slowly (here: Case II). Therefore, in Case I accelerated crystal growth occurs and needle-like growth is promoted.

The above conclusion was confirmed by evaluating the number-based median aspect ratio $AR_{50,0}$ of crystals for replicates of Case I and Case II as a function of the supersaturation at the nucleation onset S_{nucl}, which is plotted in Fig. 8. Two findings can be inferred from Fig. 8. First, the experiments with a higher evaporation rate have greater variability in S_{nucl}, and therefore worse reproducibility compared to the experiments with slow evaporation. The lowest S_{nucl} is about 1.75 and the highest over 3.50. The second finding is the obvious tendency towards the formation of more isometric crystals at lower supersaturation.

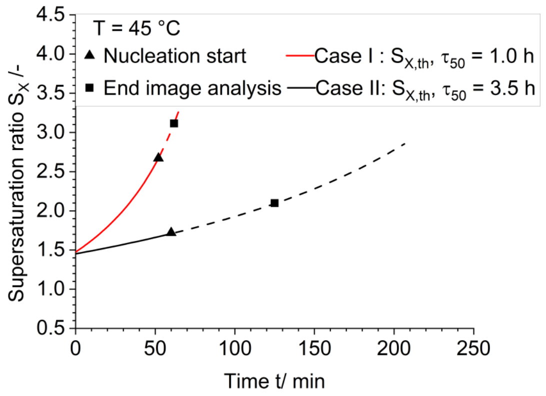

Figure 7. Calculated course of supersaturation of Bitopertin in ethanol at 45 °C for Cases I and II. The progress of the calculated supersaturation $S_{X,th}$ after nucleation onset is depicted as a dashed line. The triangles indicate the nucleation start S_{nucl} and the squares specify the time at which the final criterion of image analysis is reached.

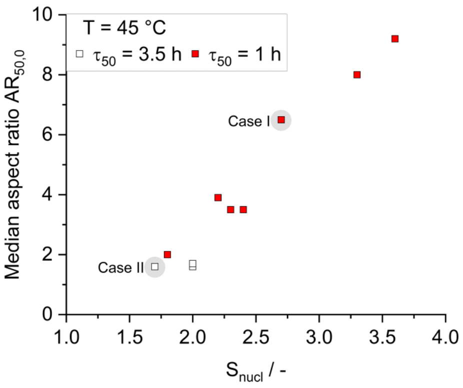

Figure 8. Number-based median aspect ratio $AR_{50,0}$ versus supersaturation at the nucleation onset S_{nucl} for replicates of the Case I (τ_{50} = 3.5 h) and Case II (τ_{50} = 1.0 h). The specific Cases I and II summarized in Tab. 1 and analyzed in Figs. 6 and 7 are highlighted in gray.

4.2.2 Effect of the Temperature (Factor 2)

Fig. 6 illustrates that the crystals of Case III exhibit an acicular habit. This case differs from Case II only in the crystallization temperature, 30 °C instead of 45 °C. However in the crystallization process, S_{nucl} of Case III is much higher in comparison with Case II (see Tab. 1), which supports again that higher supersaturation during crystallization fosters acicular growth of the Bitopertin crystals. Experiments with identical process conditions such as Case III, but with a lower supersaturation at the nucleation onset, were not observed. Among the six experiments, Case III has the lowest S_{nucl} of 2.1.

An examination of additional temperatures not listed in Tab. 1 revealed valuable insights into the effect of temperature on crystal morphology. Detailed data for these experiments are available in Sect. S11. Reducing the temperature to 15 °C while maintaining the same slow evaporation rate results in a shift in S_{nucl} to approximately 2.5, leading to the formation of acicular crystals. Consequently, at lower temperatures (30 and 15 °C), S_{nucl} and crystal growth occur at elevated levels, promoting an acicular morphology. Multiple replicates suggest that under the experimented conditions primary nucleation at lower supersaturation ratios (S_{nucl} < 2.0) is less probable at 15 and 30 °C. Conversely, elevating the temperature to 55 °C causes Bitopertin to crystallize at lower S_{nucl} values and with a more isometric shape, resembling the behavior observed at 45 °C. Experiments investigating crystallization after longer induction times at constant and lower supersaturation can truly reveal whether the temperature has a substantial effect on the crystal morphology of Bitopertin.

4.2.3 Effect of Seeding (Factor 3)

Fig. 6b highlights a significant difference in AR between Case I (without seeding) and Case IV (with seeding). In the seeded experiment, the crystal product exhibits a clear isometric morphology with AR values ranging from 1 to 5. In contrast, the equivalent case with primary nucleation shows a broad range of AR values, from 1 to 28.

Focusing on the rate of crystal formation interpreted from Fig. 9, which is based on $A_{\text{crystal}}/A_{\text{image}}$ reveals that in Case IV phase transfer begins with the start of the experiment and increases with smooth growth over time. So, from the very beginning of the experiment, the supersaturation is being depleted. In contrast, in Case II, phase transfer is much faster. As noted above, the supersaturation reaches higher values. Consequently, the system is driven to faster depletion of the supersaturation in comparison with Case IV, which has a negative impact on the uniform growth of the crystals.

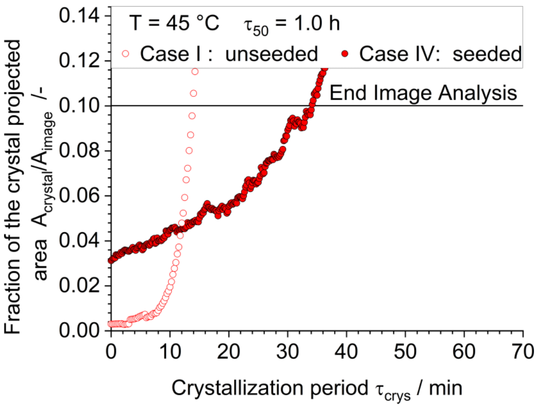

Figure 9. Ratio of the crystal projection area to the image area from nucleation onset until the end of image analysis for Cases I and IV.

4.2.4 Effect of the Solvent (Factor 4)

As can be seen in Tab. 1, the solvent also influences the modification of the crystal morphology. Under almost identical crystallization conditions ($T_c = 45\,°C$, $\tau_{50} = 3.5\,h$), acicular crystals were formed in 1-propanol (Case V) and 2-propanol (Case VI), whereas isometric crystals were observed in the equivalent experiment in ethanol (Case II).

In particular, in 1-propanol and 2-propanol, a significant difference in the onset of nucleation is observed. They have S_{nucl} values of 2.5 and 3.0, respectively, while in the case of ethanol, the nucleation started at a significantly lower S_{nucl} value of approximately 1.7. Therefore, the differences in morphologies can be explained by the same reasons given in Sects. 4.2.1–4.2.3: high supersaturation exacerbates the differences in the growth of the tips and the surrounding faces, yielding needle-shaped crystals. To understand which specific interactions are responsible for the nucleation onset occurring at higher values in 1-propanol and 2-propanol, further experiments need to be conducted, specifically focusing on the crystallization kinetics of Bitopertin.

4.3 Balapiravir and DPP-IV Inh

The same workflow was applied for Balapiravir Hydrochloride and DPP-IV Inh. Fig. 10 shows the cumulative ARs of the two APIs, representing the cases with the most and least elongated crystal morphologies. The cumulative AR distribution shows a significant effect on the crystal morphology, depending on the process conditions. The X-ray diffractograms are the same for both cases of Balapiravir and for both cases of DPP-IV Inh. Consequently, there is no change in the crystal structure in the presented cases. The modification and improvement of the crystal morphology were achieved merely through the change in crystal growth due to the different process conditions tested in the workflow. The corresponding diffractograms can be found in Sect. S10.

The crystallization studies on these two APIs reinforce the need for a rational workflow for studying crystal morphology. Even with a narrow solvent selection and a well-limited experimental design, the crystal morphologies of the selected APIs changes from highly elongated needles to more isometric crystals.

4 Conclusion

The presented experimental setup and workflow has proven to be a useful general tool for investigating and manipulating the crystal morphology of APIs with scarcely known crystallization behavior. Moreover, it fulfills key criteria, such as: (1) efficient usage of raw material by screening dozens of combinations using 200 times less raw material than typical experiments on a liter scale, (2) unmistakable assessment of the crystal morphology with the process conditions thanks to inline imaging, which facilitates the (3) possible transferability for upscaling.

Through the application of the proposed experimental setup and workflow to various APIs, specific process conditions for

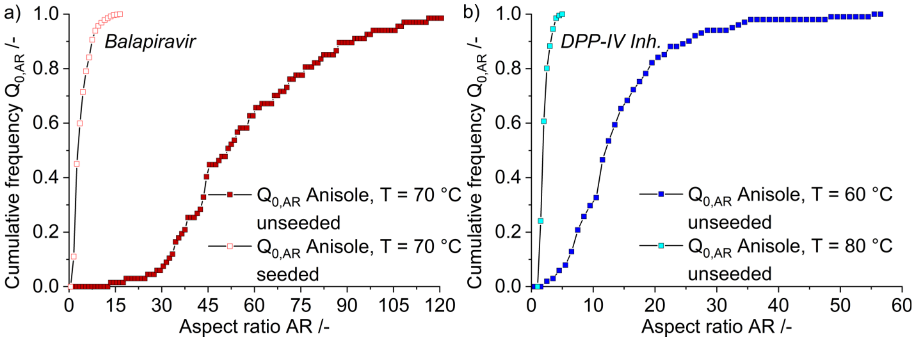

Figure 10. Particle number based cumulative distribution of the aspect ratio for the cases with the most and less elongated crystal morphologies (a) *Balapiravir Hydrochloride* (b) *DPP-IV Inh.*

each API that enhance the formation of more equant-shaped crystals were identified. Notably, by evaluating $AR_{50,0}$, a difference of at least one order of magnitude was observed between the worst and best case for each API. Furthermore, inline imaging proved to be an excellent tool for hypothesizing key relationships between crystal morphology and underlying crystallization kinetics. This is exemplified by the analysis of nucleation onset and increase in crystal area in the images acquired during crystallization. By leveraging these findings, more general strategies for achieving desired morphologies can be recommended, providing a comprehensive approach to inform decision making in the crystallization process.

In the extensively discussed case of Bitopertin, two distinct perspectives emerge: (1) From an operational standpoint, isometric crystal morphology was achieved by crystallizing Bitopertin from ethanol at 45 and 55 °C with a low evaporation rate. In contrast, crystallization from ethanol at 15 and 30 °C resulted in the formation of acicular crystals. (2) From a phenomenological viewpoint, it was noted that lower supersaturation ratios at the nucleation onset, such as those observed at 45 and 55 °C with lower evaporation rates in ethanol, promoted more isometric crystal growth. Conversely, spontaneous crystallization at higher supersaturation ratios in 1-propanol, in 2-propanol, or at lower temperatures led to acicular crystal formation. The first perspective emphasizes the required process conditions for obtaining a specific morphology, while the second opens up the possibility of hypothesizing alternative conditions that could also lead to the desired morphology.

These results, obtained at a highly miniaturized scale, also hold potential for practical use if the process conditions that yield more equant-shaped crystals prove reliable for scaling up. This topic is of utmost relevance, and we are currently preparing a second contribution that compares the findings between the miniaturized scale and liter-scale experiments.

Data Availability Statement

Further data that support the findings of this study are available on request from the corresponding author. The data are not publicly available due to privacy or legal restrictions.

Supporting Information

Supporting Information for this article can be found under DOI: https://doi.org/10.1002/ceat.202300314.

Acknowledgment

The authors wish to express their sincere gratitude to Dr. Raphael Diodone and Dr. Pirmin Hidber, representing F. Hoffmann-La Roche, for their invaluable and constructive feedback provided during the entirety of this research project. We would also like to extend our sincere appreciation to F. Hoffmann-La Roche for their generous financial sponsorship, which enabled us to carry out the necessary studies and for providing the APIs investigated in this research. Open access funding enabled and organized by Projekt DEAL.

The authors have declared no conflict of interest.

Symbols used

A_{crystal}	$[\mu m^2]$	projected area of the crystals in an image taken inline
$A_{i,j}$	[–]	first coefficient of the solubility curve
A_{image}	$[\mu m^2]$	total area of the image
$B_{i,j}$	[–]	second coefficient of solubility curve
d	[mm]	diameter
$\dot{m}$	$[\text{mg min}^{-1}]$	mass flow
m	[g]	mass
MW	$[\text{g mol}^{-1}]$	molecular weight
N_{p}	[–]	number of detected crystals in an image taken inline
Q_0	[–]	particle number-based cumulative frequency
S	[–]	supersaturation ratio
T	[°C]	temperature
t	[min]	time
X	[–]	mass loading
x	[µm]	minor/major axis of the ellipse that contours a detected crystal

Greek letters

τ_{50}	[min]	time to evaporate the half of the solvent
τ_{crys}	[min]	crystallization period

Sub- and superscripts

*	equilibrium condition
0	initial condition
50,0	particle number-based median
c	crystallization
d	dissolution
E	final state
i	solvent number
j	API number
min	minor
max	major
nucl	nucleation onset
th	calculated
v	vapor

Abbreviations

API	active pharmaceutical ingredient
AR	aspect ratio
BIR	image indicator and register
CCD	charge coupled device
CSD	crystal size distribution
DPP-IV Inh	dipeptidyl peptidase inhibitor
DSC	differential scanning calorimetry

FIC	flow indicator and controller
HAZOP	hazard and operability
ICH Q3C	international council for harmonisation of technical requirements for registration of pharmaceuticals for human use
M	mixing
MZL	metastable zone limit
PIC	pressure indicator and controller
PTFE	polytetrafluorethylene
QIR	transmissivity indicator and register
RPM	revolutions per minute
SIC	stirring indicator and controller
TIR	temperature indicator and register
TIRC	temperature indicator register and controller
XRPD	X-ray powder diffraction

References

[1] A. Cote, D. Erdemir, K. P. Girard, D. A. Green, M. A. Lovette, E. Sirota, N. K. Nere, *Cryst. Growth Des.* **2020**, *20 (12)*, 7568–7581. DOI: https://doi.org/10.1021/acs.cgd.0c00847

[2] B. Y. Shekunov, P. York, *J. Cryst. Growth* **2000**, *211 (1–4)*, 122–136. DOI: https://doi.org/10.1016/S0022-0248(99)00819-2

[3] J. Chen, B. Sarma, J. M. B. Evans, A. S. Myerson, *Cryst. Growth Des.* **2011**, *11 (4)*, 887–895. DOI: https://doi.org/10.1021/cg101556s

[4] R. J. Davey, K. Allen, N. Blagden, W. I. Cross, H. F. Lieberman, M. J. Quayle, S. Righini, L. Seton, G. J. T. Tiddy, *CrystEngComm* **2002**, *4 (47)*, 257–264. DOI: https://doi.org/10.1039/B203521A

[5] R. Beck, A. Häkkinen, D. Malthe-Sørenssen, J.-P. Andreassen, *Sep. Purif. Technol.* **2009**, *66 (3)*, 549–558. DOI: https://doi.org/10.1016/j.seppur.2009.01.018

[6] N. Pudasaini, P. P. Upadhyay, C. R. Parker, S. U. Hagen, A. D. Bond, J. Rantanen, *Org. Process Res. Dev.* **2017**, *21 (4)*, 571–577. DOI: https://doi.org/10.1021/acs.oprd.6b00434

[7] Y. Ren, J. Shen, K. Yu, C. U. Phan, G. Chen, J. Liu, X. Hu, J. Feng, *Crystals* **2019**, *9 (11)*, 556. DOI: https://doi.org/10.3390/cryst9110556

[8] S. R. Modi, A. K. R. Dantuluri, V. Puri, Y. B. Pawar, P. Nandekar, A. T. Sangamwar, S. R. Perumalla, C. C. Sun, A. K. Bansal, *Cryst. Growth Des.* **2013**, *13 (7)*, 2824–2832. DOI: https://doi.org/10.1021/cg400140a

[9] D. Hooper, F. C. Clarke, R. Docherty, J. C. Mitchell, M. J. Snowden, *Int. J. Pharm.* **2017**, *531 (1)*, 266–275. DOI: https://doi.org/10.1016/j.ijpharm.2017.08.091

[10] A. K. Tiwary, *Drug Dev. Ind. Pharm.* **2001**, *27 (7)*, 699–709. DOI: https://doi.org/10.1081/ddc-100107327

[11] A. F. Wells, *Lond. Edinb. Dublin Philos. Mag. J. Sci.* **1946**, *37 (272)*, 605–630. DOI: https://doi.org/10.1080/14786444608521520

[12] P. Hartman, W. G. Perdok, *Acta Cryst.* **1955**, *8 (1)*, 49–52. DOI: https://doi.org/10.1107/S0365110X55000121

[13] J. Prywer, *J. Cryst. Growth* **2004**, *270 (3–4)*, 699–710. DOI: https://doi.org/10.1016/j.jcrysgro.2004.06.046

[14] S. Chewle, F. Emmerling, M. Weber, *Crystals* **2020**, *10 (12)*, 1107. DOI: https://doi.org/10.3390/cryst10121107

[15] L. E. Hatcher, W. Li, P. Payne, B. Benyahia, C. D. Rielly, C. C. Wilson, *Cryst. Growth Des.* **2020**, *20 (9)*, 5854–5862. DOI: https://doi.org/10.1021/acs.cgd.0c00470

[16] R. J. Davey, *J. Cryst. Growth* **1986**, *76 (3)*, 637–644. DOI: https://doi.org/10.1016/0022-0248(86)90180-6

[17] B. Y. Shekunov, M. E. Aulton, R. W. Adama-Acquah, D. J. W. Grant, *J. Chem. Soc., Faraday Trans.* **1996**, *92 (3)*, 439–444. DOI: https://doi.org/10.1039/FT9969200439

[18] W. Omar, S. Al-Sayed, A. Sultan, J. Ulrich, *Cryst. Res. Technol.* **2008**, *43 (1)*, 22–27. DOI: https://doi.org/10.1002/crat.200710995

[19] T. T. H. Nguyen, R. B. Hammond, K. J. Roberts, I. Marziano, G. Nichols, *CrystEngComm* **2014**, *16 (21)*, 4568–4586. DOI: https://doi.org/10.1039/C4CE00097H

[20] Z. Liang, M. Zhang, F. Wu, J.-F. Chen, C. Xue, H. Zhao, *Comput. Chem. Eng.* **2017**, *99*, 296–303. DOI: https://doi.org/10.1016/j.compchemeng.2017.01.010

[21] H. Takiyama, *Adv. Powder Technol.* **2012**, *23 (3)*, 273–278. DOI: https://doi.org/10.1016/j.apt.2012.04.009

[22] A. R. Klapwijk, E. Simone, Z. K. Nagy, C. C. Wilson, *Cryst. Growth Des.* **2016**, *16 (8)*, 4349–4359. DOI: https://doi.org/10.1021/acs.cgd.6b00465

[23] R. Grimbergen, P. Bennema, H. Meekes, *Acta Crystallogr. A.* **1999**, *55 (1)*, 84–94. DOI: https://doi.org/10.1107/s0108767398008897

[24] T. Beyer, G. M. Day, S. L. Price, *J. Am. Chem. Soc.* **2001**, *123 (21)*, 5086–5094. DOI: https://doi.org/10.1021/ja0102787

[25] J. Li, C. J. Tilbury, S. H. Kim, M. F. Doherty, *Prog. Mater Sci.* **2016**, *82*, 1–38. DOI: https://doi.org/10.1016/j.pmatsci.2016.03.003

[26] N. A. Padwal, M. F. Doherty, *Cryst. Growth Des.* **2022**, *22 (6)*, 3656–3661. DOI: https://doi.org/10.1021/acs.cgd.1c01366

[27] Y. Zhao, C. J. Tilbury, S. Landis, Y. Sun, J. Li, P. Zhu, M. F. Doherty, *Cryst. Growth Des.* **2020**, *20 (5)*, 2885–2892. DOI: https://doi.org/10.1021/acs.cgd.9b01105

[28] J. Li, M. F. Doherty, *Cryst. Growth Des.* **2017**, *17 (2)*, 659–670. DOI: https://doi.org/10.1021/acs.cgd.6b01510

[29] D. S. Coombes, C. R. A. Catlow, J. D. Gale, M. J. Hardy, M. R. Saunders, *J. Pharm. Sci.* **2002**, *91 (7)*, 1652–1658. DOI: https://doi.org/10.1002/jps.10148

[30] A. R. Konak, *J. Cryst. Growth* **1973**, *22 (1)*, 67–68. DOI: https://doi.org/10.1016/0022-0248(74)90064-5

[31] T. T. H. Nguyen, T. D. Turner, A. M. E. Matinong, I. Marziano, R. B. Hammond, K. J. Roberts, *Chem. Eng. Technol.* **2021**, *44 (7)*, 1287–1293. DOI: https://doi.org/10.1002/ceat.202100025

[32] C. S. MacLeod, F. L. Muller, *Org. Process Res. Dev.* **2012**, *16 (3)*, 425–434. DOI: https://doi.org/10.1021/op200279m

[33] S. Ottoboni, M. Simurda, S. Wilson, A. Irvine, F. Ramsay, C. J. Price, *Powder Technol.* **2020**, *366*, 305–323. DOI: https://doi.org/10.1016/j.powtec.2020.02.064

[34] G. Capellades, C. Neurohr, M. Azad, D. Brancazio, K. Rapp, G. Hammersmith, A. S. Myerson, *J. Pharm. Sci.* **2020**, *109 (3)*, 1365–1372. DOI: https://doi.org/10.1016/j.xphs.2019.12.011

[35] A. K. Rajagopalan, J. Schneeberger, F. Salvatori, S. Bötschi, D. R. Ochsenbein, M. R. Oswald, M. Pollefeys, M. Mazzotti, *Powder Technol.* **2017**, *321*, 479–493. DOI: https://doi.org/10.1016/j.powtec.2017.08.044

[36] A. Bubendorf, A. Deynet-Vucenovic, R. Diodone, O. Grassmann, K. Lindenstruth, E. Pinard, F. E. Rohrer, U. Schwitter (Hoffmann-La Roche Inc), *US Patent 2008/0214561 A1*, **2008**.

[37] P. J. Harrington, S. Hildbrand, K. Sarma (F. Hoffmann-La Roche AG), *WO Patent 2008/071571 A1*, **2008**.

[38] S. Abrecht, G. Bubendorf, S. Goetzoe, O. Grassmann, F. Montavon, R. Moog, F. Rohrer, A. Ruh, M. Scalone, U. Schwitter, S. Wang (Hoffmann-La Roche Inc.), *US Patent 2006/0217428A1*, **2006**.

[39] European Directorate for the Quality of Medicines & HealthCare, *European Pharmacopoeia*, 8th ed., Council of Europe, Strasbourg **2013**.

[40] M. Allesø, F. van den Berg, C. Cornett, F. S. Jørgensen, B. Halling-Sørensen, H. L. de Diego, L. Hovgaard, J. Aaltonen, J. Rantanen, *J. Pharm. Sci.* **2008**, *97 (6)*, 2145–2159. DOI: https://doi.org/10.1002/jps.21153

[41] M. A. Reus, A. E. D. M. van der Heijden, J. H. ter Horst, *Org. Process Res. Dev.* **2015**, *19 (8)*, 1004–1011. DOI: https://doi.org/10.1021/acs.oprd.5b00156

Research Article: A miniaturized multi-reactor system and knowledge-based workflow were developed to identify optimal process conditions for controlling the crystal morphology of active pharmaceutical ingredients (APIs). This method, which features minimal material usage, inline imaging, and independent control of temperature *T* and supersaturation *S*, can be used to obtain more equant-shaped crystals of diverse APIs.

A Comprehensive Workflow towards More Equant-Shaped Crystals of Active Pharmaceutical Ingredients

Nicolás Ramos Ojeda, Matthias Kind*

Chem. Eng. Technol. **2024**, *47 (XX)*, XXX … XXX

DOI: 10.1002/ceat.202300314

Supporting Information available online